Excitation of rotons in parahydrogen crystals: The laser-induced-molecular-alignment mechanism

Johan Lindgren and Toni Kiljunen*

Department of Chemistry, Nanoscience Center, P. O. Box 35, FI-40014 University of Jyväskylä, Finland

(Received 30 May 2013; published 17 October 2013)

Solid parahydrogen (p-H_2) is known to support long-lived coherences, of the order of 100 ps, which enables high-resolution spectroscopy in the time domain. Rotational Raman-type excitations to sublevels of $J = 2$ are delocalized due to electric-quadrupole–quadrupole coupling in p-H_2 crystals, and the resulting states can be characterized as rotons. Wave packets of rotons exhibit molecular alignment with respect to laboratory coordinates. Here the concept of field-free molecular alignment, induced by strong ultrashort laser pulses, is extended into a molecular solid case. We derive a solid-state analog for the gas-phase alignment measure and illustrate the time-dependent alignment degree in p-H_2 crystals by numerical simulations. To underscore the Raman gain effect of the solid, general properties of the field-free alignment are revisited by comparing gaseous p-H_2 with N_2. The interplay between the polarization direction of the excitation pulses and the axis directionality of the crystal is shown to affect the alignment dynamics via the spatial ($M = 0, \pm1, \pm2$) composition of the roton wave packets. We simulate experimental traces by incorporating the induced alignment degree in the calculation of heterodyne-detected realization of femtosecond pump-probe optical Kerr effect spectroscopy. With the help of dispersed, two-dimensional resolved images of the calculated signal we reproduce the experiment as a whole. To that end, the effects of probe chirp, shape, and power must be explored in detail. We find good agreement with previous experiments and unravel the ambiguity of tracing back the wave-packet composition from the signal; in particular, we find that the effect of quantum phase factors of all the components should be taken into account when explaining the signal properties.

DOI: 10.1103/PhysRevA.88.043420 PACS number(s): 42.50.Md, 42.50.Hz, 78.47.J−, 82.53.Xa

I. INTRODUCTION

Controlling the direction of molecular bonds by moderately intense laser pulses has been the topic of a significant amount of experimental and theoretical activity [1,2]. The basic physics of intense-field alignment of gas-phase molecules is now well understood. It is generally favorable to utilize short, nonresonant laser pulses instead of an adiabatic excitation with a static electric field. Then, possible side effects due to electric field are suppressed as long as the ionization or other thresholds of sample breakdown processes are not crossed. In this dynamic, field-free regime, oscillating alignment results due to formation of a wave-packet state. It exhibits a transient postpulse alignment due to rotational revival structure. Spatial aspects of alignment depend on the polarization of the laser field that interacts with the anisotropic molecular polarizability. Molecules can become aligned with respect to a given space-fixed axis by choosing a linear or a circularly polarized field. Three-dimensional alignment, to force molecules into a plane or to suppress rotations completely, must use elliptical polarization or a suitable combination of laser pulses [2–4]. Advanced control methods to manipulate rotations in three dimensions (3D) include multipulse schemes [5–7] and optimal control theory [8,9], with interesting outcomes such as molecular cogwheels [10] and stopwatches [11]. Having reached a relatively mature state, the concept of molecular alignment has already been manifested in a variety of applications, resulting in fascinating demonstrations of fundamental molecular physics in the gas phase [12–14].

In condensed phase the topic of quantum control has advanced only recently [15,16]. The motivation lies in the unique properties of rotationally broad wave packets that can be utilized as sensitive probes of the dissipative properties [17,18] and the energy level structure [19] of the environment. Rotational Raman transitions underlying the induced alignment process can be used themselves to study intermolecular forces. Molecular hydrogen is a suitable probe due to relatively weak interactions and its simple structure [20,21]. As a coherence-based control tool, efficient extension of the alignment mechanism to the condensed phase is posing challenges both experimentally and theoretically [22–25]. Therefore, parahydrogen (p-H_2) as a minimally perturbing quantum condensed phase makes natural sense as the media to study. Particularly appealing is the manifestation of long-lived condensed-phase coherence by relaxation of rotational excitation (roton) [26,27]. In the presence of one $J = 2$ roton in solid p-H_2, there is one molecule in the $J = 2$ rather than in the $J = 0$ state. The states in this $J = 2$ band form a traveling rotational excitation; i.e., the total angular momentum is located at a different molecule at different times [28]. The $J = 2$ band is split due to anisotropic intermolecular forces, and the main interaction originates from electric-quadrupole–quadrupole (EQQ) coupling between the relatively distant hydrogen molecules [28]. Thus, elastic collisions or fluctuations of the EQQ interactions are the main source of dephasing, and, apart from energy level splitting, p-H_2 molecules behave as free rotors. These nearly free rotors possess a large zero point motion as the quantum solid property, and as a consequence are insignificantly affected by lattice vibrations (phonons).

A rotational coherence that lasts more than 12 ps was revealed by femtosecond pump-probe 2D optical Kerr effect (OKE) spectroscopy in recent p-H_2 experiment [27]. The

*toni.k.kiljunen@jyu.fi

 ©2013 American Physical Society

coherent oscillation of a ca. 94-fs period originates from the $J = 2 \leftarrow 0$ excitation $S_0(0)$ that can be categorized as a creation of delocalized rotons. The method relies on the pump laser-induced birefringence in the solid. The signal appears as stimulated Raman side bands of the probe pulse, while the Raman-active optical phonon mode exhibits a ca. 900-fs oscillation period at the probe center. A closer examination with higher resolution revealed a splitting into $|M| = 0,1,2$-state substructure, where three components with 93.7-, 94.2-, and 94.8-fs oscillation periods can be resolved along with their mutual quantum beats [29,30]. The refined experiments also reported extended dephasing times T_2 on the order of 100 ps, a value which is controlled by the purity with respect to orthohydrogen concentration [30,31]. The extent of delocalization for the roton-type excitation in the solid parahydrogen is another interesting point accessible to evaluation by the impurity dependence [30].

Here, we report quantum simulations together with an illustrative experimental signal. We have chosen to highlight the nonresonant alignment point of view as the underlying mechanism in OKE spectroscopy. This leads to the extension of the alignment concept from the gas phase to condensed phase (molecular solids). Theoretical foundations of solid p-H_2 are well known [28] and rotational Raman spectra of the solid have also been thoroughly considered [32–34]. Although the transverse optical phonon part of the signal is a very prominent feature in the experiments [27,29,30], it is left out of the discussion by assuming negligible interplay of phonon and roton dynamics. These elementary excitations have a tenfold energy mismatch and a fivefold difference in dephasing time [30]. Phonon sidebands are only a very weak feature in rotational Raman spectra, and rotational excitations are strongly decoupled from intramolecular vibrations, too [35]. Furthermore, roton lifetimes are independent of temperature, which eliminates possible influence of lattice vibrations [26]. We use this information to incorporate the bulk solid effect into the alignment scheme and resolve the labor of implementing the EQQ and the three reference frames: laboratory (laser fields), crystal, and molecule. The emphasis is put on the geometric aspects in light-molecule interaction. We present the dependence of the roton excitation on the polarization direction of the field relative to the hexagonal direction of the crystal. In particular, the purpose of the paper is to reproduce computationally and explain the recent experimental spectra [27,29]. The present theoretical work provides insights that cannot easily be gained from experiments alone. In connection with the experiments [27], we also felt that the H_2 molecule itself deserved more attention. Therefore, we report a brief gas-phase survey, where the alignment process is worked out much in the same manner as in previous N_2 studies [12,36–48], elaborating on the differences in the high-B (rotational constant), small-$\Delta\alpha$ (anisotropy of polarizability) molecule H_2 as compared to the N_2.

II. EMPIRICAL BACKGROUND

Parahydrogen crystals grown in closed copper cells are large and transparent with regular shapes and known orientations of the hcp single crystals. Although cubic centimeter scale single crystals with zero birefringence can be grown,

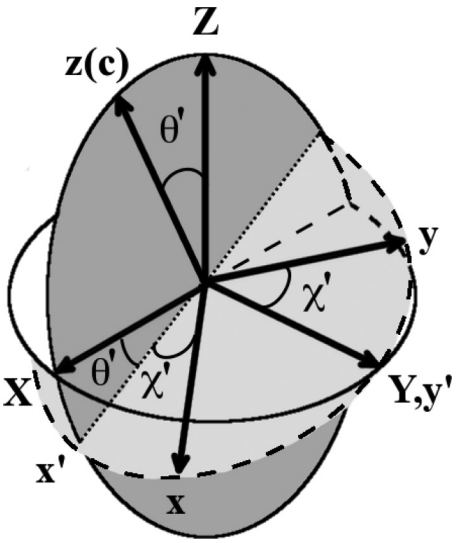

FIG. 1. Definition of the relative orientations of crystal (x,y,z) and laboratory (X,Y,Z) axes by Euler angles, where Z is the polarization direction of the pump laser field and c labels the principal axis of the hcp crystal frame. The laser beams propagate in the Y direction. The crystal frame is shown after operation $R_{y'}(\theta')$, where rotation by an angle θ' occurs in the ZX plane (dark gray). After $R_z(\chi')$, the crystal axes (x,y) are rotated by an angle χ' relative to x',y' (light gray).

we consider crystals grown in cylindrical cells, where the c axis points radially from the copper wall towards the center of the cylinder [27,29]. The radial orientation of the c axis with respect to the linearly polarized excitation laser field (Z) then depends on the location where the beam enters the cell; see Fig. 1 for definition of the angular coordinate system. In order to sample a unique c-axis direction by the excitation and probe laser pulses, the collinear beam propagation direction Y is aligned with the cylinder axis, which is perpendicular to c axis and therefore to the ZX laboratory plane. This choice sets the Euler angle $\phi' = 0$. The long crystal cell dimensions (ca. 3 cm) are necessary to prevent damage of the windows on the cell due to use of focused ultrafast laser beams. Along the beam path within the crystal the angle χ' can, in principle, be randomly distributed among single crystallites. However, the beams are focused such that only a volume of cubic millimeter scale is sampled, ensuring that the signal is dominantly generated from one single crystal in each experiment [27,29,30].

The OKE spectroscopy is a pump-probe polarization spectroscopy, also called as time-resolved Raman-induced Kerr effect spectroscopy (RIKES) [49] or Raman-induced polarization spectroscopy (RIPS) [50,51], where a pump-induced birefringence is detected through its influence on the probe pulse polarization. The linearly polarized pump pulse, nonresonant with any molecular eigenstate of the system, excites the Raman-active modes that lie in the bandwidth of the pulse via a stimulated Raman scattering. The tensorial aspects of nonlinear polarization have been analyzed by Morgen *et al.* [51] regarding the RIPS in the weak-field limit. The tensorial properties of the molecular response and consequent optical polarization in the sample lead to induced anisotropy. The polarization of an initially linearly polarized weak probe pulse, delayed by a time interval with respect to the pump pulse,

acquires an elliptic component which can pass the analyzer set perpendicular to the probe polarization [52]. Molecular alignment is a direct measure of the induced birefringence $\Delta n(t)$, which is the difference of refractive indices between parallel (extraordinary) and perpendicular (ordinary) directions in the sample with respect to the axis defined by the pump polarization. The oscillation of the alignment degree encodes the energy level structure and coherence in the signal by modulating the detected intensity. The formulation behind the detected signal is given in Sec. III C.

III. THEORY

We consider the molecular rotational energy structure in the solid parahydrogen subject to the interaction with the aligning laser pulse, and the consequent coupling of the exciton ($J = 2$ roton) states via the EQQ interaction in the crystal. Ignoring dissipation effects in the rotational alignment, the Hamiltonian for the system reads

$$H(t) = H_0 + H_c + H_{\rm ind}(t), \tag{1}$$

where

$$H_0 = B_0 \sum_i J_i(J_i+1) - D_0 \sum_i J_i^2(J_i+1)^2 \tag{2}$$

represents the free quantum rotors with molecular angular momentum J_i. The rotational parameters have values $B_0 = 59.322\ \mathrm{cm}^{-1}$ and $D_0 = 0.0471\ \mathrm{cm}^{-1}$ in the gas phase [53]. These values must be scaled in order to reproduce the OKE signal from the solid p-H_2.

The crystal-field Hamiltonian H_c is derived in Sec. III A, where we also give the split energy levels that result from diagonalizing H_c in Bloch-type states. The crystal consists of N para molecules with their centers of mass fixed at the sites of a regular hcp lattice with $N/2$ unit cells. The wave functions are functions of the orientations of the N molecules. The crystal states consist of the ground state, which is a product state of all molecules in the $J = 0$ rotational state, and singly excited states, where one of the molecules (i) is in a $J = 2, M$ state:

$$|\psi_{Mi\gamma}\rangle = |Y_{00}(1)\rangle \cdots |Y_{2M}(i,\gamma)\rangle \cdots |Y_{00}(N)\rangle, \tag{3}$$

where γ labels the site (α or β) within the unit cell. The functions $|Y_{JM}\rangle$ are spherical harmonics with M referring to the hexagonal axis of the crystal. The wave functions of rotational energy bands are linear combinations of the $N(2J+1)$ functions given in Eq. (3). The proper combination symmetry is fulfilled by the Bloch functions [54]

$$|\psi_M(\mathbf{k})\rangle^{\pm} = N^{-1/2} \sum_i \exp(i\mathbf{k}\cdot\mathbf{R}_i)[|\psi_{Mi\alpha}\rangle \pm |\psi_{Mi\beta}\rangle]. \tag{4}$$

It is essential to restrict to the $\mathbf{k} \approx 0$ wave vector region of the Brillouin zone, where the even and odd states do not mix. Furthermore, only transitions to even exciton states $|\psi_M(0)\rangle^+$ are Raman active. For each value of M, the exciton has an equal probability to be found at any of the site locations $\mathbf{R}_i$. The kinetic energy operator $H_0 + H_c$ reduces to diagonal $H_{\rm cry}$

$$H_{\rm cry} = H_0 + E_M(0)^+, \tag{5}$$

where the energy $E_M(0)^+$ represents the lattice sum of the anisotropic components of the intermolecular potential. In this treatment, other states than single $J = 2$ excitations coupled to $J = 0$ are disregarded. Double excitations of pairs of molecules, such as to form a $|J_1 J_2\rangle = |22\rangle$ crystal state, are very weak (of the order of phonon side bands) in Raman spectra [35] and appear at ca. $12B_0$, which is outside the laser pulse widths used in impulsive Raman processes of this work (see below). Moreover, $\Delta J = 4$ transitions are reported two orders of magnitude lower in intensity than $\Delta J = 2$ [55] and sequential $J = 4 \leftarrow 2$ pumping probability also suffers from the $14B_0$ energy difference.

The basis set actually used in the calculation of the time-dependent alignment in the crystalline p-H_2 consists of the $|JM\rangle$ rotational eigenstates of isolated molecules. The equivalent in the coordinate space is the set of spherical harmonics $Y_{JM}(\theta,\phi)$. We thus abandon the crystal state description only needed to obtain the known level structure in Sec. III A. The case is analogous to a matrix-isolated impurity molecule, and the EQQ interactions are pairwise summed to yield a quantum crystal-field effect. Technically, we consider a localized case instead of the traveling exciton, but we retain the term roton for the wave packet. The probe pulse can be thought to propagate along with the roton wave throughout the sample and thus be affected in each region of the crystal in a uniform way [27].

The induced Hamiltonian (derived in Sec. III B) is dependent on the relative orientation of the crystal with respect to the laser polarization, which in turn dictates the M-level composition. The quantum state is expanded as

$$|\Psi_{\rm rot}(t)\rangle = \sum_{JM} c_{JM}(t)|JM\rangle. \tag{6}$$

The numerical task then is to integrate the time-dependent Schrödinger equation,

$$\frac{d|\Psi_{\rm rot}(t)\rangle}{dt} = -\frac{i}{\hbar}[H_{\rm cry} + H_{\rm ind}(t)]|\Psi_{\rm rot}(t)\rangle, \tag{7}$$

in the rotational basis of Eq. (6) using an explicit Runge-Kutta formula. Based on the moderately low intensity of the laser field, we can restrict to $J_{\max} = 2$ here. The corresponding 6×6 Hamiltonian matrices are evaluated analytically and implemented in the numerical wave-packet propagation code. While expanding the basis to $J = 4$ and computing the matrix elements of $H_{\rm ind}$ and the expectation values related to the signal field would be rather straightforward, developing the corresponding crystal field theory would increase the workload significantly.

In the gas-phase case, the angle θ is between the molecular symmetry axis and polarization direction of the laser (laboratory instead of a crystal frame) and becomes the sole angular variable in the expression for the induced Hamiltonian. For the gaseous p-H_2 and N_2 molecules, we propagate in Sec. IV A the density matrix $\rho_{\rm rot}(t) = |\Psi_{\rm rot}(t)\rangle\langle\Psi_{\rm rot}(t)|$ directly in the Liouville-von Neumann formalism [18],

$$\frac{d\rho_{\rm rot}(t)}{dt} = -\frac{i}{\hbar}\left[H_0 + H_{\rm ind}(t), \rho_{\rm rot}(t)\right], \tag{8}$$

to account for the distribution of initial states at 80 K. Basis set size can be set to a low value ($J_{\max} \sim 10$), since $J = 4$

state amplitude is practically zero for p-H_2 with the present pulse durations and intensities. We report the time evolution without any dissipation effects. The expectation value of $\cos^2\theta$ is used as the time-dependent degree of alignment and is obtained as

$$\langle\langle\cos^2\theta\rangle\rangle(t) = \mathrm{Tr}\{\cos^2\theta\,\rho_{\mathrm{rot}}(t)\}. \tag{9}$$

The trace can further be divided into population and coherence parts: $\langle\langle\cos^2\theta\rangle\rangle = \langle\langle\cos^2\theta\rangle\rangle_p + \langle\langle\cos^2\theta\rangle\rangle_c$, which account for the time evolution of the diagonal and off-diagonal elements of the density matrix, respectively. For a random ensemble, the average of the alignment degree equals the isotropic value of 1/3. The offset from this value is contained in the diagonal part of the density matrix, while the off-diagonal elements represent coherences between molecular eigenstates and show oscillation with respect to the population part. The partitioning opens a direct way to separable measurements of the population decay and the loss of phase coherence [17,56].

A. Crystal-field effect

We employ the spherical tensor formulation for the electrostatic interaction between the molecules. Starting from the spherical harmonic addition theorem [57] one finds the following expansion in a global coordinate system [58]

$$\begin{aligned} H_c = \frac{1}{2}\sum_{i\neq j}\frac{1}{4\pi\epsilon_0}\sum_{l_1l_2}\sum_{m_1m_2m}(-1)^{l_1}\left[\frac{(2l_1+2l_2+1)!}{(2l_1)!(2l_2)!}\right]^{1/2} \\ \times \hat{Q}^{(i)}_{l_1m_1}\hat{Q}^{(j)}_{l_2m_2}R_{ij}^{-l_1-l_2-1}C_{l_1+l_2,m}(\hat{R}_{ij}) \\ \times \begin{pmatrix} l_1 & l_2 & l_1+l_2 \\ m_1 & m_2 & m \end{pmatrix}, \end{aligned} \tag{10}$$

where $C_{lm} = \sqrt{4\pi/(2l+1)}Y_{l,m}$ are renormalized spherical harmonics, $\hat{Q}_{lm}$ are multipole moment operators, and the Wigner $3j$ symbols are defined by

$$\begin{aligned} &\begin{pmatrix} l_1 & l_2 & l_3 \\ m_1 & m_2 & m_3 \end{pmatrix} \\ &\quad = (2l_3+1)^{-1/2}(-1)^{l_1-l_2-m_3}\langle l_1m_1l_2m_2|l_3-m_3\rangle. \end{aligned}$$

The Coulomb interactions are additive, so one can sum over the distinct i,j pairs separated by distances R_{ij} with relative directions $\hat{R}_{ij}$. The multipole moment operators can be expressed in local coordinates by substituting

$$\hat{Q}_{lm} = \sum_k D^{(l)*}_{m,k}\hat{Q}_{lk} \tag{11}$$

and replacing operators with expectation values. The electric quadrupole moments are the main contribution to anisotropic forces in solid hydrogen, so one restricts to $l_1 = l_2 = 2$ terms. Moreover, the linear molecule has Cartesian quadrupole moment components $\Theta_{xx} = \Theta_{yy} = -\Theta_{zz}/2$ so that the only nonzero spherical component is $Q_{20} = \Theta_{zz} \equiv Q$, and $k = 0$. Noting that the Wigner function for rotation is related to the spherical harmonics by $D^{(l)*}_{m,0}(\phi,\theta,\chi) = \sqrt{4\pi/(2l+1)}Y_{l,m}(\theta,\phi)$, the Hamiltonian term becomes

$$\begin{aligned} H_c = \frac{1}{2}\sum_{i\neq j}\frac{\sqrt{70}}{\epsilon_0}\frac{Q^2}{5R_{ij}^5}\sqrt{\frac{4\pi}{9}}\sum_{m_1m_2}Y_{2,m_1}(i)Y_{2,m_2}(j) \\ \times C(224,m_1m_2)\,Y^*_{4,m_1+m_2}(\hat{R}_{ij}), \end{aligned} \tag{12}$$

where $C(224,m_1m_2)$ is a Clebsch-Gordan coupling coefficient. The operators $Y_{2,m}$ depend on the dynamical variables θ_i,ϕ_i of the molecular axis with respect to the crystal, while the functions $Y_{4,m}$ are numerical factors determined by the relative positions of the molecule pairs in the crystal.

Choosing a central molecule i with $\mathbf{R}_i = 0$, the summation is carried over the hexagonal lattice to give the energy levels of the $J = 2$ roton band split by $E_M(0)^+$ as [54]

$$E_M(0)^+ = 0.903\frac{Q_0^2}{5R_e^5}\begin{cases} 6, & M = 0, \\ 1, & |M| = 2, \\ -4, & |M| = 1, \end{cases} \tag{13}$$

where $R_e = 3.783$ Å is the nearest-neighbor distance [59] and $Q_0 = 0.4858\,ea_0^2$ is the quadrupole moment [28]. The $S_0(0)$ Raman triplet splitting to $M = \pm1,\pm2,0$ follows predominantly from the quadrupolar interaction, and the local van der Waals effects in the crystalline field can be neglected. Together with the unperturbed (gas-phase) $E_2 = 6B_0 - 36D_0$ energy of a $J = 2$ level, the first-order treatment of H_c yields three Raman frequency shifts [$S_0(0)$ transition] at 352.1, 354.8, and 357.4 cm^{-1} in M-state order of $|M| = 1,2,0$. To find good agreement with experimental values [29] of 351.98, 353.99, and 356.00 cm^{-1}, it was necessary to adjust the molecular constants. The final set of parameters is $B_0 = 59.319$ cm^{-1}, $D_0 = 0.0646$ cm^{-1}, and $Q_0 = 0.4352$ a.u. These give a numerical value of 0.402 cm^{-1} for the crystal-field strength.

B. Laser-field interaction

The nonresonant laser field causing the exciton formation interacts with the molecules via the polarizability of the medium [2],

$$H_{\mathrm{ind}}(t) = -\tfrac{1}{2}\mathcal{E}(t)\cdot\alpha\cdot\mathcal{E}(t), \tag{14}$$

where the polarizability is equal to the sum of the polarizabilities of the separate molecules, $\alpha = \sum_i \alpha(\mathbf{R}_i)$. In terms of spherical tensors, the dipole-dipole polarizability can be written as [58]

$$\alpha_{m,m'} = \sum_n \frac{\langle n_i|\hat{\mu}_m|n\rangle\langle n|\hat{\mu}_{m'}|n_i\rangle + \langle n_i|\hat{\mu}_{m'}|n\rangle\langle n|\hat{\mu}_m|n_i\rangle}{\mathcal{E}_n - \mathcal{E}_{n_i}}, \tag{15}$$

where $\hat{\mu}_m$ is the $m = 1,0,-1$ component of the dipole moment operator, and the states $|n_i\rangle = |\xi_i\nu_i\rangle$ and $|n\rangle = |\xi\nu\rangle$ stand for the ground and excited vibronic state manifolds, respectively, with electronic states labeled as ξ and the corresponding vibrational states as ν. It is convenient to construct a tensor product from $\alpha_{m,m'}$, which transforms according to angular momentum labels L and M [57],

$$\alpha^L_M = \sum_{mm'}\langle 1m1m'|LM\rangle\alpha_{m,m'}, \tag{16}$$

where $\langle 1m1m'|LM\rangle \equiv C(11L,mm')$. For the linear molecules only α_0^0 and α_0^2 components exist. These can be denoted by the symbols $\overline{\alpha} = -\alpha_0^0/\sqrt{3}$ and $\Delta\alpha = \sqrt{3/2}\alpha_0^2$ for the mean polarizability and anisotropy, respectively, which are given by relations $\overline{\alpha} = (\alpha_\parallel + 2\alpha_\perp)/3 = (\alpha_{zz} + \alpha_{xx} + \alpha_{yy})/3$ and $\Delta\alpha = \alpha_\parallel - \alpha_\perp = \alpha_{zz} - (\alpha_{xx} + \alpha_{yy})/2$. With these definitions, the field-induced part of the Hamiltonian becomes

$$\begin{aligned} H_{\rm ind} &= -\frac{1}{2}\sum_{mm'} \alpha_{-m,-m'}\mathcal{E}_m\mathcal{E}_{m'}(-1)^{m+m'} \\ &= -\frac{1}{2}\sum_{mm'}\sum_L \langle 1-m\,1-m'|L\ -(m+m')\rangle \\ &\quad\times \alpha^L_{-(m+m')}\mathcal{E}_m\mathcal{E}_{m'}(-1)^{m+m'} \\ &= -\frac{1}{2}\sum_{mm'}\sum_L \langle 1-m\,1-m'|L\ -(m+m')\rangle \\ &\quad\times \alpha^{L*}_{m+m'}\mathcal{E}_m\mathcal{E}_{m'}. \end{aligned} \tag{17}$$

For the isotropic, $L = 0$ part we have

$$\begin{aligned} H^{(0)}_{\rm ind} &= -\frac{1}{2}\sum_{mm'}\langle 1-m\,1-m'|00\rangle\alpha_0^{0*}\mathcal{E}_m\mathcal{E}_{m'}\delta_{m,-m'} \\ &= -\frac{1}{2}\sum_{m}\langle 1-m\,1m|00\rangle\alpha_0^{0*}\mathcal{E}_m\mathcal{E}_{-m} \\ &= -\frac{1}{2}\left(-\frac{1}{\sqrt{3}}\right)\alpha_0^{0*}\sum_m(-1)^m\mathcal{E}_m\mathcal{E}_{-m} = -\frac{1}{2}\overline{\alpha}\mathcal{E}^2. \end{aligned} \tag{18}$$

For the $L = 2$ part we obtain

$$\begin{aligned} H^{(2)}_{\rm ind} &= -\frac{1}{2}\sum_{mm'}\langle 1-m\,1-m'|2\ -(m+m')\rangle\alpha^{2*}_{m+m'}\mathcal{E}_m\mathcal{E}_{m'} \\ &= -\frac{1}{2}\sum_{mm'}C(112,mm')\alpha^{2*}_{m+m'}\mathcal{E}_m\mathcal{E}_{m'}. \end{aligned} \tag{19}$$

So far everything is defined in the crystal frame. We want to define the electric field of the laser in the laboratory coordinates and use the polarizability components known for the molecule in the body-fixed frame. Referring to the molecule, we write the anisotropic polarizability in terms of the Euler angles (ϕ,θ,χ) as

$$\alpha^2_{m+m'} = \sum_M D^{(2)*}_{m+m',M}(\phi,\theta,\chi)\alpha^2_M = D^{(2)*}_{m+m',0}(\phi,\theta,\chi)\alpha^2_0, \tag{20}$$

where the latter equality results since only the α_0^2 exists in the body-fixed frame. Using $D^{(2)*}_{m+m',0}(\phi,\theta,\chi) = \sqrt{4\pi/5}Y_{2,m+m'}(\theta,\phi)$, we obtain the following form for the interaction:

$$\begin{aligned} H_{\rm ind} &= -\frac{1}{2}\sqrt{\frac{8\pi}{15}}\Delta\alpha\sum_{mm'}C(112,mm')Y^*_{2,m+m'}(\theta,\phi)\mathcal{E}_m\mathcal{E}_{m'} \\ &\quad -\frac{1}{2}\overline{\alpha}\mathcal{E}^2. \end{aligned} \tag{21}$$

For the field terms we rotate the laboratory frame Cartesian components to the crystal frame, thus specifying the angles (ϕ',θ',χ'), and apply the Cartesian to spherical tensor transformation $(xyz) \to (1,0,-1)$. We denote the former by a rotation matrix Φ and the latter by a transformation matrix $\mathbf{U}$ [57],

$$\mathbf{U} = \begin{pmatrix} -1/\sqrt{2} & -{\rm i}/\sqrt{2} & 0 \\ 0 & 0 & 1 \\ 1/\sqrt{2} & -{\rm i}/\sqrt{2} & 0 \end{pmatrix}, \tag{22}$$

and write

$$\mathcal{E}^{\rm cryst}_m = \sum_r U_{mr}\mathcal{E}^{\rm cryst}_r, \quad \mathcal{E}^{\rm cryst}_{m'} = \sum_s U_{m's}\mathcal{E}^{\rm cryst}_s, \tag{23}$$

$$\mathcal{E}^{\rm cryst}_r = \sum_R \Phi_{rR}\mathcal{E}^{\rm lab}_R, \quad \mathcal{E}^{\rm cryst}_s = \sum_S \Phi_{sS}\mathcal{E}^{\rm lab}_S. \tag{24}$$

With linearly polarized pump field along the laboratory coordinate Z, only the column

$$\Phi_{rZ} = \begin{pmatrix} -\sin\theta'\cos\chi' \\ \sin\theta'\sin\chi' \\ \cos\theta' \end{pmatrix} \tag{25}$$

is needed, and the field is defined as

$$\mathcal{E}(t) = \tfrac{1}{2}(\varepsilon_Z e^{-{\rm i}\omega t} + \varepsilon^*_Z e^{{\rm i}\omega t}). \tag{26}$$

The field product term in Eq. (21) then obtains the following form:

$$\mathcal{E}_R\mathcal{E}_S = \tfrac{1}{4}\left(\varepsilon_Z\varepsilon^*_Z + \varepsilon^*_Z\varepsilon_Z + \varepsilon^2_Z e^{-2{\rm i}\omega t} + \varepsilon^{2*}_Z e^{2{\rm i}\omega t}\right) = \tfrac{1}{2}|\varepsilon_Z|^2, \tag{27}$$

where the oscillatory terms are neglected and the intensity envelope is contained implicitly; i.e., $\varepsilon_Z = \varepsilon(t)$.

In the coordinate system depicted in Fig. 1, the field-molecule interaction Hamiltonian $H_{\rm ind}$ takes the following five-term expansion:

$$\begin{aligned} H_{\rm ind} &= -\tfrac{1}{4}\varepsilon(t)^2\Delta\alpha\times\Big[Y_{2,0}\sqrt{16\pi/45}\left(\cos^2\theta' - \tfrac{1}{2}\sin^2\theta'\right) \\ &\quad + (Y_{2,2} + Y_{2,-2})\sqrt{2\pi/15}\sin^2\theta'(\cos^2\chi' - \sin^2\chi') \\ &\quad + (Y_{2,1} - Y_{2,-1})\sqrt{8\pi/15}\sin\theta'\cos\theta'\cos\chi' \\ &\quad + i(Y_{2,2} - Y_{2,-2})\sqrt{8\pi/15}\sin^2\theta'\sin\chi'\cos\chi' \\ &\quad + i(Y_{2,1} + Y_{2,-1})\sqrt{8\pi/15}\sin\theta'\cos\theta'\sin\chi'\Big], \end{aligned} \tag{28}$$

where the θ',χ'-dependence is explicit. The matrix elements are readily evaluated in spherical harmonics basis [57]. We have used a short-hand notation $Y_{2,M} \equiv Y_{2,M}(\theta,\phi)$. By setting $\theta' = \chi' = 0$ in Eq. (25), i.e., $r = s = z$ and $U_{mz} = (0,1,0)^{\rm T}$ [Eq. (22)], the laboratory and crystal frames coincide, and Eq. (28) reduces to the familiar (gas-phase) form,

$$\begin{aligned} H^{\rm gas}_{\rm ind} &= -\frac{1}{4}\varepsilon(t)^2\left[\sqrt{\frac{8\pi}{15}}\Delta\alpha C(112,00)Y^*_{2,0}(\theta,\phi) + \overline{\alpha}\right] \\ &= -\frac{1}{4}\varepsilon(t)^2\left[\Delta\alpha\left(\cos^2\theta - \frac{1}{3}\right) + \overline{\alpha}\right] \\ &= -\frac{1}{4}\varepsilon(t)^2(\Delta\alpha\cos^2\theta + \alpha_\perp), \end{aligned} \tag{29}$$

where θ is again the angle between the molecular axis and the polarization direction of the laser. The prefactor term

$\varepsilon(t)^2\Delta\alpha/4$ offers a control for the extent of the rotational excitation via the pulse duration and intensity. The employed laser pulse $\varepsilon(t)$ is a Gaussian of the form

$$\varepsilon(t) = \varepsilon_a e^{-2\ln 2\,(t/\sigma)^2}, \tag{30}$$

where ε_a is the laser-field amplitude, the intensity $\mathcal{I}$ (TW/cm^2) follows from the relation $\varepsilon_a^2 = 2\mathcal{I}/\varepsilon_0 c$, and σ is the pulse duration (FWHM of pulse intensity) in ps. The anisotropy of polarizability $\Delta\alpha$ was set to a constant value [60] of 0.30 Å^3, which is by a factor of three lower than that for N_2 (0.89 Å^3) [61].

C. Signal-field detection

We begin with the density matrix $\rho_{\rm rot}(t)$ resulting from the pump-pulse interactions, which contains 6×6 elements $|JM\rangle\langle J'M'|$ in the rotational basis $\{|00\rangle, |2\pm 1\rangle, |2\pm 2\rangle, |20\rangle\}$. When treating the OKE spectroscopy as a four-wave mixing technique, the system interacts twice with the pump pulse ($k_1 = k_2$) and is nonintrusively interrogated with the probe pulse (k_3) at delay time τ after the pump. The pump-induced rotational density has only coherence terms $|2M\rangle\langle 00|$ and $|00\rangle\langle 2M|$, which can be assigned to two different third-order responses R_{ijkl} [62]. The coherent Raman scattering signal is detected in the direction of the probe: $\mathbf{k}_s = \mathbf{k}_1 - \mathbf{k}_2 + \mathbf{k}_3$. Although the interaction strength with intense pump pulses goes beyond the perturbative regime, the theoretical framework relies on expanding in powers of the electric field. Consideration of the $J = J' = 2$ elements, such as $|22\rangle\langle 22|$ population or $|22\rangle\langle 21|$ coherence, involves a fifth-order process (six-wave mixing), where the signal still propagates along the probe as the pump accounts for the first four directionally canceling interactions, twice from the ket and twice from the bra side of the Feynman diagram, before the probe interaction. Adapting from Mukamel [62–64], we write the density operator in the form

$$\rho(t) = \sum_{e,mnn'} [|gn\rangle\rho_{gn,gn'}(t)\langle gn'| + |em\rangle\rho_{em,gn'}(t)\langle gn'|], \tag{31}$$

where n and m are rovibrational quantum numbers in the ground (g) and excited (e) electronic states, respectively. With nonresonant pump pulses, the $\rho_{gn,gn'}(t)$ represent the doorway states which interact with the time-delayed probe pulse, conceptionally creating virtual-state coherences $\rho_{em,gn'}(t)$. The dynamics resides in the ground electronic state. The equation of motion for density matrix elements $\rho_{gn,gn'}$ is given by effective Hamiltonian in Eq. (8), and time-dependent properties such as molecular alignment can be readily obtained.

We concentrate on times after the pump-induced creation of the $\rho_{\rm rot}$ [being part of $\rho_{gn,gn'}(t)$ state space] and consider this nonequilibrium density matrix as the initial state $\rho(t_0 = 0)$ interrogated by the well-separated probe field (acting to ket from the left)

$$\mathcal{E}_p(t) = \varepsilon_p(t-\tau)\hat{\epsilon}_p e^{-i\omega_p(t-\tau)}. \tag{32}$$

The material response to applied laser fields is imprinted in the optical polarization $P(t;\tau)$, which is the expectation value of the dipole operator $\hat{\mu}$ dictated by the density matrix:

$$P_{nn'}(t;\tau) = \mathrm{Tr}\{\hat{\mu}\rho(t,\tau)\} + \text{c.c.} \tag{33}$$

$$= \int_{t_0}^{t} d\tau' \mathcal{E}_p(\tau')\frac{i}{\hbar}\mathrm{Tr}\{\hat{\mu}(t)\hat{\mu}(\tau')\rho_{gn,gn'}(t_0)\} + \text{c.c.} \tag{34}$$

The time propagation of the density matrix is here brought by the dipole operator $\hat{\mu}$ in the interaction picture:

$$\hat{\mu}(t) = e^{\frac{i}{\hbar}H_{\rm cry}(t-t_0)}\sum_{nm}[\mu_{nm}|gn\rangle\langle em| + \mu_{mn}|em\rangle\langle gn|]e^{-\frac{i}{\hbar}H_{\rm cry}(t-t_0)}, \tag{35}$$

where $\mu_{mn} = \langle em|\hat{\mu}|gn\rangle$. Successive operations to $\rho_{gn,gn'}(0)$ yield the signal source as mediated by the vibronic polarizability tensor:

$$\begin{aligned} P_{nn'}(t;\tau) &= \int_0^t d\tau' \mathcal{E}_p(\tau')\frac{i}{\hbar}\mathrm{Tr}\left\{\sum_m \mu_{n'm}\mu_{mn}e^{-i(\omega_{em}-\omega_{gn})(t-\tau')}\rho_{\rm rot}(t)\right\} \\ &= \int_0^t d\tau' \varepsilon_p(\tau'-\tau)e^{i\omega_p(\tau-t)}\mathrm{Tr}\left\{\sum_m \frac{i}{\hbar}\mu_{n'm}\mu_{mn}e^{i(\omega_p-\omega_{em,gn}+i\gamma_{eg})(t-\tau')}\hat{\epsilon}_p\rho_{\rm rot}(t)\right\} \\ &= \varepsilon_p(t-\tau)e^{-i\omega_p(t-\tau)}\mathrm{Tr}\left\{\sum_m \frac{\mu_{n'm}\mu_{mn}}{\hbar(\omega_p-\omega_{em,gn}+i\gamma_{eg})}\hat{\epsilon}_p\rho_{\rm rot}(t)\right\} = \varepsilon_p(t-\tau)e^{-i\omega_p(t-\tau)}\mathrm{Tr}\{\alpha(\omega_p)\hat{\epsilon}_p\rho_{\rm rot}(t)\}, \end{aligned} \tag{36}$$

where instantaneous decay ($\gamma_{eg}\to\infty$) is used and the complex conjugate is not written for the intermediate steps to Eq. (36). The result includes the Kramers-Heisenberg-Dirac expression for the dynamic polarizability $\alpha(\omega_p)$ similar to Eq. (15). Due to the initial state weighting by coefficients $c_{JM}c^*_{J'M'}$, we can restrict to $J \neq J'$ so that the polarization has Raman shifts $\omega_p \pm \omega_{nn'}$ where plus and minus mean $|2M\rangle\langle 00|$ (anti-Stokes) and $|00\rangle\langle 2M'|$ (Stokes) branches, respectively. The trace is over the rotational manifold.

The system response is detected by a square-law detector after mixing the signal field $E_s = i(\omega_p l/c)P(t;\tau)$ with a local oscillator $E_{\rm lo}$, resulting in a heterodyne-detected signal. The nonlinear refraction is dependent on the pump intensity $\mathcal{I}$ as $n(\mathcal{I}) = n_0 + n_2(\mathcal{I})$, which introduces the multiplicative term

where l is the optical length of the focus volume and c the speed of light. Self-heterodyning is achieved experimentally by turning the probe pulse polarization by an angle $\vartheta \approx 1^\circ$ from exactly crossed polarizer-analyzer geometry. A portion of the probe field amplitude then penetrates the analyzer even when no birefringence is present in the medium: $E_{\rm lo} = \sin\vartheta\, \mathcal{E}_p(t)\exp(i\varphi_{\rm lo})$. Since the total intensity is $I = |E_s + E_{\rm lo}|^2$, we have $I = |E_s|^2 + 2{\rm Re}\{E_s E_{\rm lo}^*\} + |E_{\rm lo}|^2 = I_{\rm hom} + I_{\rm het} + I_{\rm lo}$, respectively. The time-integrated homodyne signal is written as

$$I_{\rm hom}(\tau) = \left(\frac{\omega_p l}{c}\right)^2 \int_{-\infty}^{\infty} dt\, \varepsilon_p^2(t-\tau) \times [{\rm Tr}\{[\hat{\epsilon}_A \cdot \alpha(\omega_p)\hat{\epsilon}_p]\rho(t)\}]^2. \quad (37)$$

The homodyne part is a positive quantity as it measures only the deviation from the isotropy. The heterodyne part is

$$I_{\rm het}(\tau) = 2\frac{\sin\vartheta\, \omega_p l}{c} \int_{-\infty}^{\infty} dt\, \varepsilon_p^2(t-\tau) \times {\rm Tr}\{[\hat{\epsilon}_A \cdot \alpha(\omega_p)\hat{\epsilon}_p]\rho(t)\}. \quad (38)$$

The heterodyne-detected signal can have positive and negative values, and it carries the phase information of the signal field. The local oscillator intensity $I_{\rm lo}$ is time independent and only brings a background to the signal:

$$I_{\rm lo} = \sin^2\vartheta \int_{-\infty}^{\infty} dt\, \varepsilon_p^2(t). \quad (39)$$

Experimentally, the pump pulse is polarized in the Z direction, the probe pulse is oriented at $(45+\vartheta)^\circ$ with respect to the pump pulse: $\hat{\epsilon}_p \approx (-1,0,1)^{\rm T}/\sqrt{2}$ in the X,Y,Z-frame, and the analyzer is oriented nearly perpendicular to probe's initial polarization: $\hat{\epsilon}_A = (1,0,1)^{\rm T}/\sqrt{2}$. The analyzer selects a component of the induced dipole moment so that the detected molecular response is proportional to the scalar product of polarization vectors: $\hat{\epsilon}_A \cdot \alpha(\omega_p)\hat{\epsilon}_p$. Expressing the probe-induced vibronic polarizability in molecular frame, $\alpha^{\rm (lab)} = \Phi^{-1}\alpha^{\rm (mol)}\Phi$, and multiplying with the directions of the probe and analyzer, we obtain

$$\hat{\epsilon}_A \cdot \alpha(\omega_p)\hat{\epsilon}_p = \frac{\Delta\alpha}{2}[\cos^2\theta - \cos^2\phi\sin^2\theta]. \quad (40)$$

The angle θ is the angle between laser polarization direction and the molecular axis and ϕ is the azimuthal angle. The expression is the same as derived by Renard *et al.* [65], except for $\cos^2\phi$ instead of $\sin^2\phi$. However, the trace operation removes the ϕ dependence in the gas phase, and one obtains

$$A_\gamma^{\rm (gas)}(t) = \frac{\Delta\alpha}{2}[\langle\cos^2\theta\rangle(t) - 1/3]e^{-\gamma t} \quad (41)$$

for the trace. Thus, the usual measure for alignment degree is very suitable for characterization of the birefringence-dependent OKE signal.

In the case of solid parahydrogen, we denote the angles by capital letters to distinguish from the crystal frame coordinates. We denote the solid-state alignment degree function by $A_\gamma(t)$,

$$A_\gamma(t) = \frac{\Delta\alpha}{2}[\langle\cos^2\Theta\rangle - \langle\cos^2\Phi\sin^2\Theta\rangle](t)e^{-\gamma t}, \quad (42)$$

where the decay function with $1/\gamma = 90$ ps is added to account for the loss of rotational coherence. It is convenient to rotate the operator $Y_{2,0}(\Theta,\Phi)$ to make the crystal and laboratory frames to coincide:

$$\begin{aligned}\langle\cos^2\Theta\rangle &= \frac{1}{3} + \sqrt{\frac{16\pi}{45}}\langle Y_{2,0}(\Theta,0)\rangle \\ &= \frac{1}{3} + \sqrt{\frac{16\pi}{45}}\sum_{M'} D^{(2)*}_{0,M'}(\phi'=0,\theta',\chi')\langle Y_{2,M'}(\theta,\phi)\rangle \\ &= \frac{1}{3} + \sqrt{\frac{16\pi}{45}}\sum_{M'} d^{(2)}_{0,M'}(\theta')e^{iM'\chi'}\langle Y_{2,M'}(\theta,\phi)\rangle. \quad (43)\end{aligned}$$

We have used the arguments mentioned in Sec. III B to set Euler angle $\phi' = 0$ and used the explicit form of the Wigner D matrices [57]. To obtain the result for the gas-phase alignment, the operator $Y_{2,0}(\Theta,0)$ is replaced with $Y_{2,0}(\theta,\phi)$. Similarly, we have

$$\langle\cos^2\Phi\sin^2\Theta\rangle = \sqrt{\frac{2\pi}{15}}[\langle Y_{2,2}(\Theta,\Phi)\rangle + \langle Y_{2,-2}(\Theta,\Phi)\rangle] + \frac{1}{3} - \frac{1}{2}\sqrt{\frac{16\pi}{45}}\langle Y_{2,0}(\Theta,0)\rangle, \quad (44)$$

where

$$Y_{2,\pm2}(\Theta,\Phi) = \sum_{M'} d^{(2)}_{\pm2,M'}(\theta')e^{iM'\chi'}Y_{2,M'}(\theta,\phi). \quad (45)$$

To reiterate, the final expression for solid-state alignment is implemented as

$$A_\gamma(t) = \frac{\Delta\alpha}{2}\sum_{M'} e^{i\chi' M'}\langle Y_{2,M'}(\theta,\phi)\rangle(t)e^{-\gamma t} \times \left\{\sqrt{\frac{4\pi}{5}}d^{(2)}_{0,M'}(\theta') - \sqrt{\frac{2\pi}{15}}\left[d^{(2)}_{2,M'}(\theta') + d^{(2)}_{-2,M'}(\theta')\right]\right\}. \quad (46)$$

We scale the OKE signal intensity by $[\omega_p l/c]^{-2}$ to obtain the final implemented form:

$$I(\tau) = \int dt\, \varepsilon_p^2(t-\tau)\left[A_\gamma^2(t) + 2C A_\gamma(t) + C^2\right]. \quad (47)$$

The local oscillator amplitude is defined through the value of $C = \sin\vartheta\, c/\omega_p l$. When $C = 0$, the signal is homodyne detected and it beats at the inverse of difference (and sum) frequencies $\omega_{MM'}$. When C is large, we observe the transition frequencies ω_M. We set C suitably between the above limits.

In order to simulate the experiments [27,29] as a whole, we also produce spectrally dispersed signals. The intensity collected by a spectrometer is

$$I(\omega,\tau) = \left|\int_{-\infty}^{\infty} dt e^{i\omega t}[E_{\rm lo}(t) + E_s(t;\tau)]\right|^2, \quad (48)$$

which we implement in the form

$$I(\omega,\tau) = \left|\int dt e^{i\omega t}\varepsilon_p(t-\tau)A_\gamma(t)\right|^2 - 2{\rm Re}\left\{E_{\rm lo}^*(\omega)\int dt e^{i\omega t}\varepsilon_p(t-\tau)A_\gamma(t)\right\}. \quad (49)$$

The two terms in Eq. (49) are the homodyne (left) and the heterodyne (right) parts of the signal, and the local oscillator intensity is neglected. The probe carrier frequency is also eliminated in the Fourier transforms. The shape of the local oscillator is modified from that of the probe due to the wavelength dependence of the polarizer-analyzer extinction ratio. In particular, the probe center wavelength is suppressed the most, leading to a double-peak shape of the local oscillator [29]. We simulate this effect by implementing the field in a self-phase-modulated form [66]:

$$E_{\rm lo}(\omega) = C \int dt e^{i\omega t} \varepsilon_p(t-\tau) i e^{i\pi[\varepsilon_p(t-\tau)]^2}. \qquad (50)$$

Effects of linear chirp are included by multiplying the probe function in Eq. (32) by $\exp[-ic'(t-\tau)^2]$, where $c' = -45\ \mathrm{ps}^{-2}$ is the chirp rate applied here.

IV. SIMULATION RESULTS

A. Gas-phase alignment for p-H_2 and N_2

The rotational excitation occurs via the stimulated nonresonant Raman process in the time-resolved femtosecond pump-probe OKE spectroscopy. As the present pulses have durations in the fs scale, below the rotational period $\tau_{\rm rot}$, the study falls in the category of nonresonant, field-free alignment. In this regime, a short pulse generally excites a broad wave packet in the angular space, which then spreads and at certain times, called revival times, the spreading fully reverses and molecular alignment is observed; see Fig. 2. The rephasing time is usually defined as the average energy between rotational states, $T_{\rm rev} \equiv \tau_{\rm rot} = 1/2Bc$, where B is the rotational constant [2]. The alignment can also exhibit fractional revival times, originating from the coherence in copies of the original wave packet, and are observed in the case of the N_2 [47].

We demonstrate the time-dependence of the alignment degree in hydrogen and compare the result with another homonuclear molecule, N_2. The expectation value of the squared cosine in the rotational wave packet for the parahydrogen gas is shown in Fig. 2(a). We chose a pump-pulse duration of 40 fs (FWHM) with intensity of 10 TW/cm^2 for the pulse parameters as these values produce nearly the same degree of alignment for both the H_2 and the N_2. The rotational temperature is set to 80 K, which matches the temperature in the recent numerical and experimental studies on N_2 [47,48]. The time dependence of the alignment is rather simple for p-H_2, as the $J = 2$ state is not initially populated at low temperatures and the field intensities considered here do not extend the rotational excitation to the $J = 4$ state. Therefore, the coherence part $\langle\langle\cos^2\theta\rangle\rangle_c$ oscillates at the inverse of the rotational frequency 355 cm^{-1} and the population part $\langle\langle\cos^2\theta\rangle\rangle_p$ is close to the isotropic limit. This mapping of the alignment degree corresponds to a heterodyne-detected signal.

Using the same experimental parameters for N_2 gas, a revival pattern of alignment emerges with $\tau_{\rm rot} \approx 8.4$ ps in Fig. 2(b). Because the odd and even J states are unevenly populated (even states contribute twice as much as odd states), alignment is also observed at quarter and three-quarter revival times. At 80 K, the highest thermally populated state is $J = 4$, according to the Boltzmann statistics. As the nonresonant

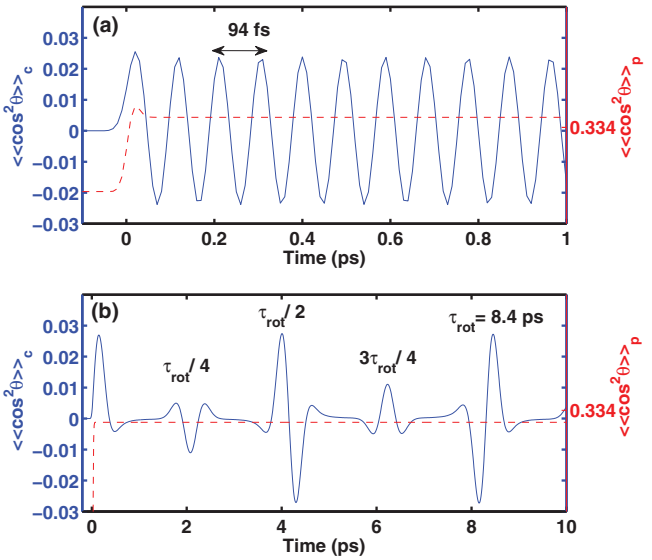

FIG. 2. (Color online) Alignment degree decomposed to the $\langle\langle\cos^2\theta\rangle\rangle_c$ (solid line, left axis) and $\langle\langle\cos^2\theta\rangle\rangle_p$ (dashed line, right) parts in gaseous parahydrogen (a) and nitrogen (b) with 40 fs (FWHM) pulse duration and 10 TW/cm^2 intensity at 80 K. (a) Coherent oscillation of 94 fs period results from the rotational transition $J = 2 \leftarrow 0$, with most of the wave-packet population in the $J = 0$ state. (b) Alignment structure that arises from the localization and relocalization of the wave packet is shown up to the first full revival time $\tau_{\rm rot} = 8.4$ ps. The fractional revivals $\tau_{\rm rot}/4 = 2.1$ ps, $\tau_{\rm rot}/2 = 4.2$ ps, and $3\tau_{\rm rot}/4 = 6.3$ ps are marked in the figure. The quarter and three-quarter revival times are peculiar to homonuclear diatomics and originate from the spin statistics. The present experimental parameters lead nearly to the same degree of alignment contrast for both molecules.

pulse excites the rotational states via the Raman $\Delta J = \pm 2$ transitions, the resulting rotational wave packet is significantly broader in the J space than the equivalent in the case of hydrogen. In the Fourier transform of the signal, peaks at $2B_0(2J+3)$ separated by $4B_0$ (neglecting the centrifugal term) would be observed.

At the zero temperature limit, an order of magnitude estimate for the maximum rotational state $J_{\rm max}$ in the wave packet can be given: With short and intense laser pulses, the coupling strength Ω_R and pulse duration σ dictate the extent of rotational excitation as $J_{\rm max} \sim \sigma\Omega_R$. With long and low intensity pulses, a proportionality relation $J_{\rm max} \sim \sqrt{\Omega_R/2B_e}$ is more suitable [67]. The coupling strength, referred as Rabi coupling, is $\Omega_R^{JJ'} = \frac{1}{4}\varepsilon_m^2 \Delta\alpha \langle J|\cos^2\theta|J'\rangle$. In addition to the J dependence of the Rabi coupling, the interaction strength is proportional to field intensity and anisotropic polarizability.

The postpulse alignment degree is seen to degrade in Fig. 3(a), if longer pump pulses are used for p-H_2. At the adiabatic limit, the alignment degree returns to the isotropic value of 1/3 after the pulse has gone. The adiabatic condition is generally met at $\sigma \approx \tau_{\rm rot} = 1/2Bc$, which for p-H_2 is 280 fs. Here, however, the 94-fs observed period necessitates significantly shorter pulses. At $\sigma = 120$ fs, the system is already close to adiabatic behavior. Simultaneous decrease in the expectation value of $J(J+1)$ is observed in Fig. 3(b). The

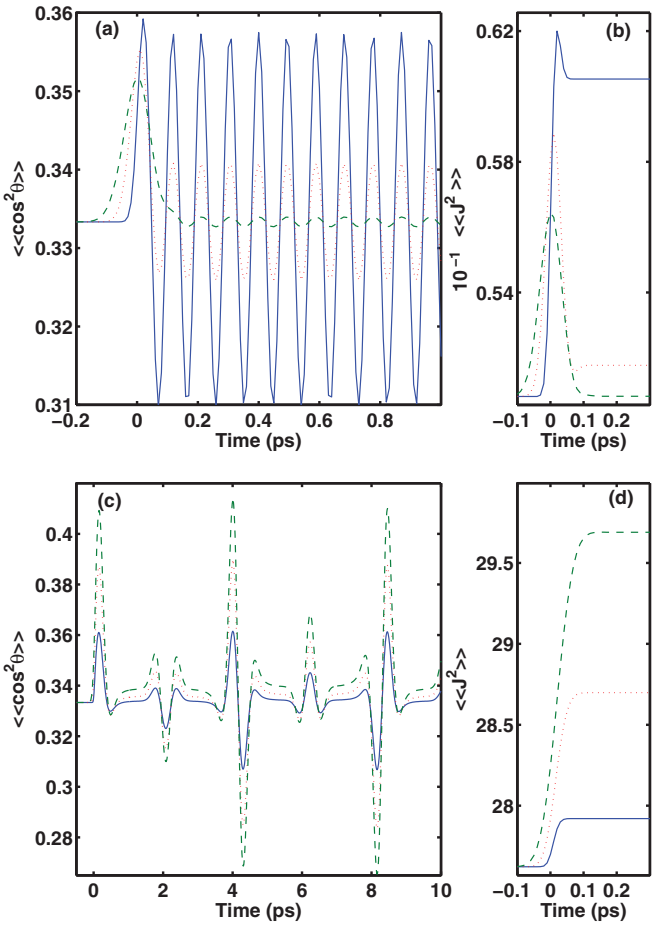

FIG. 3. (Color online) Impact of the $I = 10$ TW/cm^2 pulse length on alignment degree in p-H_2 (a),(b) and N_2 (c),(d) at 80 K. (a) Modulation amplitude of the alignment and (b) extent of the rotational excitation $\langle\langle J^2 \rangle\rangle$ degrade as functions of the pulse duration σ: 40 fs (solid blue line), 80 fs (dotted, red line), and 120 fs (dashed, green line). The $\sigma = 120$ fs case is near the adiabatic limit where alignment is lost after the pulse. (c),(d) Inverse trend is observed for N_2 where the relation $J_{\max} \propto \sigma \Omega_R$ applies.

same simulation for nitrogen shows different behavior, which results from the order-of-magnitude difference in the rotational parameters. The alignment enhances as the interaction time under the pump-pulse envelope is elongated; see Fig. 3(c). Here, the molecule experiences an increase in the number of Rabi-type cycles. Along with the increase in alignment degree, the expectation value of the $J(J+1)$ in the wave packet increases in Fig. 3(d). As the pulse duration is increased, with the chosen pulse intensity, the relation $J_{\max} = \sigma \Omega_R$ gives qualitatively correct behavior for the rotational excitation in nitrogen.

B. Alignment in p-H_2 crystals

We investigated the impact of laser pulse properties on the (gas-phase) alignment in the previous section. Here, we take on a different approach and consider the pump-probe OKE signal with a single set of pulse parameters: a moderate pump length of 100 fs and lower peak intensity of 1.0 TW/cm^2. We solve Eq. (7) to obtain the wave packet [Eq. (6)]. Due to the low temperature in experiments (4–11 K), we can consider the system initially in a pure state. The pump-pulse duration is set shorter than what was measured [29], since simulations with the experimental 166-fs duration go too far in the adiabatic regime to clearly reproduce oscillating alignment as the result of wave-packet dynamics. In the 100-fs case, although the amplitude c_{20} reaches 3.2×10^{-3} at the peak of the pulse (for $\theta' = \chi' = 0$), it drops during the Gaussian pulse down to zero before setting to the postpulse value of 3.4×10^{-4}. The node region also resets the phases φ_M. The state coefficients can be divided into probability and quantum phase terms as [68] $c_{2M}(t) = \sqrt{p_M(t)} \exp[-i(\varphi_M(t) + \omega_M t)]$, where the angle dependence is implicit.

The induced Hamiltonian [Eq. (28)] derived in Sec. III B reveals the role of angular variables θ' and χ' in the excitation of a rotational wave packet. We assume that single c-axis direction is sampled within the volume of the pump focus, thereby picking a single angle θ'. Referring to the coefficients $|c_{J|M|}|^2 = |c_{JM}|^2 + |c_{J-M}|^2$ in the roton wave packet in Fig. 4, we can predict the weights of the crystal-field split frequencies in OKE signals. For example, if we choose $\theta' = 54°$, the transition frequency to the $M = 0$ substate (solid, blue line) should disappear from the signal. In case of $\theta' = 77°$, the $|M| = 2$ substate (dot-dashed, green line) should dominate the signal over the other substates that have nearly equal weights. The squared quantities $|c_{J|M|}|^2$ do not show χ' dependence; they manifest only the θ' control. The overall amplitude of the $J = 2$ excitation is also seen to depend on θ', which modulates the sum $(\sum |c_{2|M|}|^2)$ normalized to the value at $\theta' = 0°$. The state distribution exhibits mirror symmetry for angles θ' higher than shown in Fig. 4.

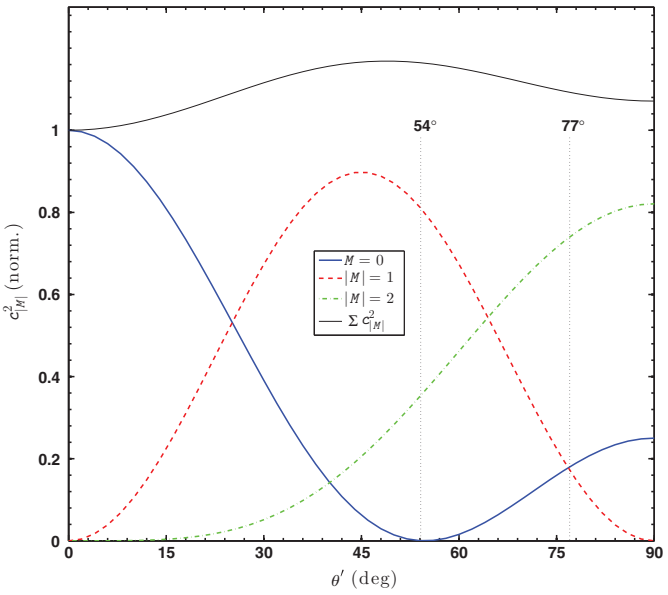

FIG. 4. (Color online) $|M|$-state distribution of the roton wave packet as a function of orientation (θ') of the c axis with respect to polarization of the pump field. The coefficients are normalized to $c_{20}^2 = 1.1 \times 10^{-7}$ at $\theta' = 0°$. Vertical lines indicate the two orientations chosen for demonstration of the roton state selection, which affects the alignment degree and OKE.

The initial quantum phase of the $|20\rangle$ component is $\varphi_0(0) = \pi/2$, when $(\cos^2\theta' - 0.5\sin^2\theta')$ is positive, and $-\pi/2$ otherwise. The phases of other $J = 2$ components develop in parallel during the pulse, thus maintaining the relative difference. The initial phase, however, varies with both the angles according to Eq. (28). The expectation values relevant to alignment degree and signal detection show a variable phase relation in contrast to the gas-phase case. It should be noted that the degenerate $\pm M$ coefficients can differ in phase φ_M, although their amplitude $\sqrt{p_M}$ is the same. For example, setting $\theta', \chi' = 77°, 0°$, we have $\varphi_0 = \varphi_{-1} = -\pi/2$ and $\varphi_2 = \varphi_{-2} = \varphi_1 = \pi/2$; i.e., there are zero and π phase shifts between the wave-packet components.

Since the orientation χ' within a pump focus volume cannot be controlled, we scan this angle for the two representative values of θ'. For the $\theta' = 54°$ case, Fig. 5(a) shows the Fourier transform of signal intensity,

$$I(\omega;\chi') = \int d\tau\, e^{i\omega\tau} I(\tau;\chi') \tag{51}$$

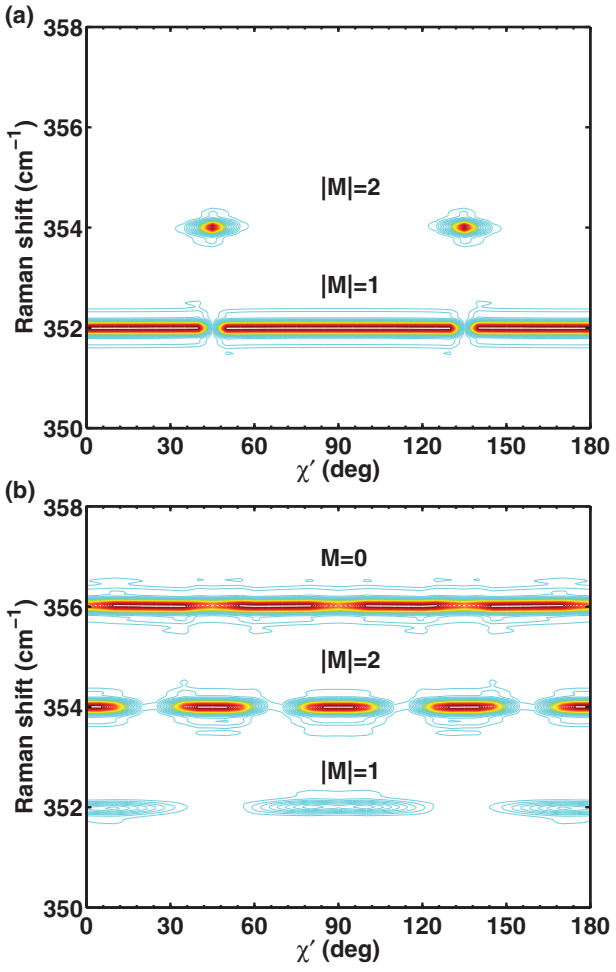

FIG. 5. (Color online) Spectral representation of χ' dependence in the solid-state alignment degree. The c axis is oriented at (a) 54° or (b) 77° with respect to the pump pulse. The $M = \pm 1$ or $M = \pm 2$ substates emerge, respectively, as the dominant components over the relative intensities, which can be tracked to the wave-packet coefficients shown in Fig. 4.

[see Eq. (47)], where the probe envelope function was replaced with $\delta(t - \tau)$. Self-heterodyning was obtained by setting $C = 0.003$, and C^2 was subtracted. Also, the homodyne part was dropped for plotting purposes. The spectrogram results from 160-ps-long propagations of $\rho(t;\chi')$ using $1/\gamma = 90$ ps for the dephasing time. The χ' dependence appears as a structure in the $|M| = 1$ and $|M| = 2$ components resolved at 352 and 354 cm^{-1}, respectively. As predicted, the $M = 0$ state is not observed at any angle χ'. The variation of the expectation value as a function of χ' implies the complex-valued influence of the crystal orientation to the detection of roton wave-packet composition. The angle dependence arises from the operator $\cos^2\Theta - \cos^2\Phi \sin^2\Theta$ instead of the $H_{\rm ind}$; see Eqs. (42)–(46) and (28), respectively.

In Fig. 5(b) we change the polarization direction of the excitation pulse to $\theta' = 77°$ in order to have all the three components visible. The χ' modulation results from the alignment observable A_γ and interference effects. The oscillations are out of phase, which influences the emergence of the weak component $|M| = 1$. For example, at $\chi' = 90°$, where $|M| = 2$ has a maximum, the spectral density of $|M| = 1$ is suppressed due to destructive interference. The same happens for $M = 0$, which deviates from constant intensity at the $|M| = 2$ maxima. The interference is controlled by the dephasing time that hinders the resolution of the quantum beats. The $|M| = 0,1$ components exhibit minor weight in the spectral density with respect to the dominant $|M| = 2$, as predicted in Fig. 4. An extreme amplitude contrast is obtained at $\chi' = 0°$, for example. However, by picking the local minimum of $|M| = 2$ intensity at $\chi' = 20°$, we can invert the dominance in favor of $M = 0$. These two values of χ' are used in the following presentations of the time-resolved OKE signals.

From the M populations in Fig. 4 we know which $|M|$ substates are contributing to the oscillating alignment degree and to the OKE signal field. The choice of χ' controls the emergence of the components in the detection scheme. Figure 6 presents the results for $\theta', \chi' = 77°, 0°$. The alignment degree is related to the OKE signal intensity by Eq. (47). The parameters are the same as in Fig. 5, except the probe envelope is included with $\sigma = 130$ fs. The trace in Fig. 6(a) consists of the heterodyne-detected intensity, with the 94-fs oscillation period of the $J = 2$ roton and of the homodyne-detected intensity modulation with oscillation period of 16.7 ps: $\tau_{\rm osc} = 2\pi/(\omega_2 - \omega_1) = 2\pi/(\omega_0 - \omega_2)$, where $\omega_1 = 351.98\,{\rm cm}^{-1}$, $\omega_2 = 353.99\,{\rm cm}^{-1}$, and $\omega_0 = 356.00\,{\rm cm}^{-1}$. The first intensity maximum coincides with the electronic response at $\tau = 0$ and the recursions occur exactly at multiples of $\tau_{\rm osc}$. The locations of maxima are related to phase shifts between the wave-packet components, as shown below. The homodyne contribution shows twice as fast dephasing as the heterodyne component due to the square dependence on the alignment degree. The local oscillator intensity C^2 is again removed from the total signal intensity. If we increase the probe duration, the number of 94-fs oscillation cycles under the probe envelope increases and the modulation averages out. By pulses much shorter than 130 fs, the signal intensity modulation shows an increasing heterodyne component with the 94-fs time period. The Fourier transform of the trace in panel (b) shows the fast components at frequencies 352, 354, and 356 cm^{-1}. The

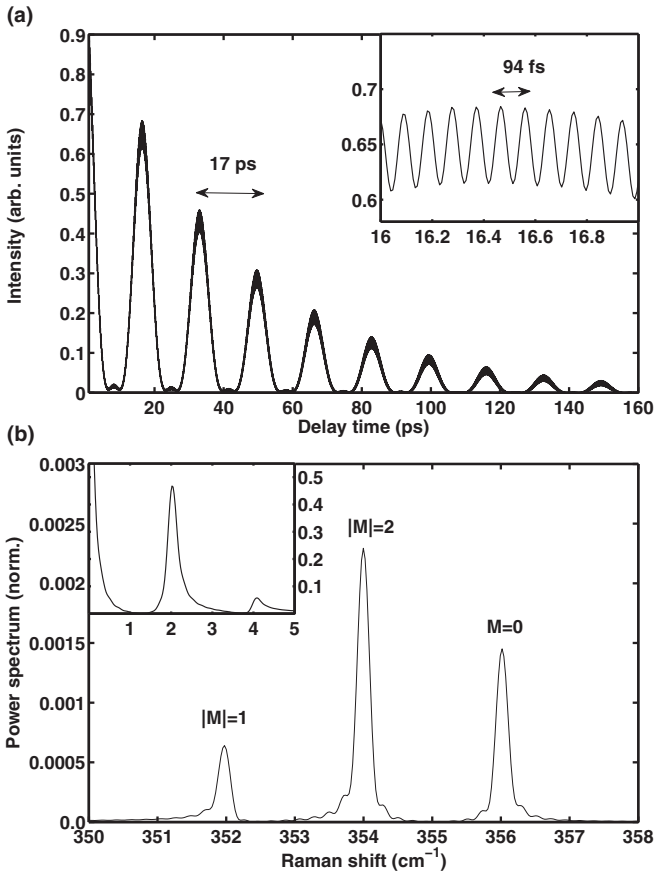

FIG. 6. (a) Numerical representation of the OKE signal calculated using Eq. (47) for $\theta' = 77°, \chi' = 0°$. The inserted 1-ps interval of the signal resolves the roton oscillation period of 94 fs. (b) Spectral density resolving the $|M|$-state distribution of the Raman transition: rotational frequencies at 352, 354, and 356 cm^{-1}. The inset resolves the difference frequency at 2 cm^{-1} originating from the homodyne-detected part of the signal. Probe duration was set to $\sigma = 130$ fs, dephasing time to $\gamma^{-1} = 90$ ps, and local oscillator strength to $C = 0.003$.

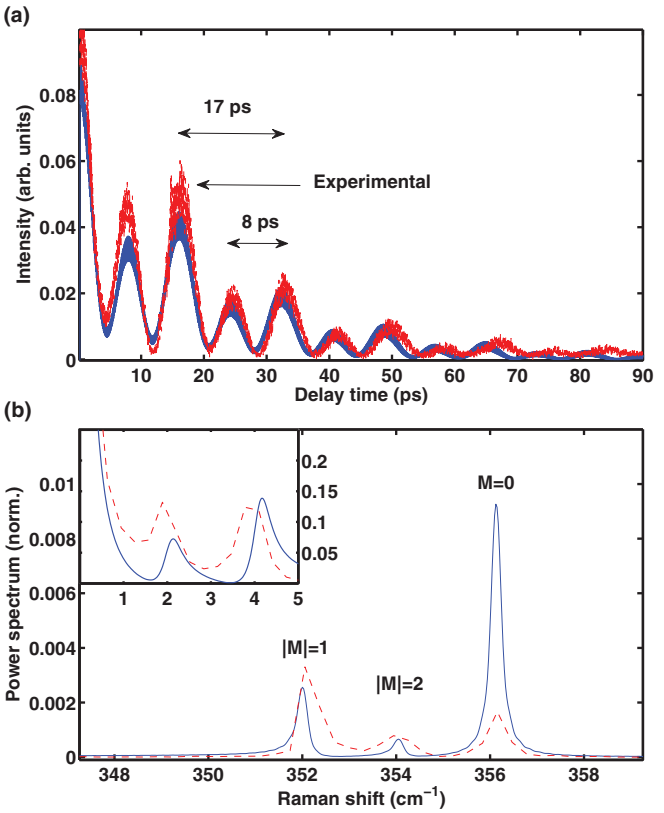

FIG. 7. (Color online) Comparison of simulated $\theta' = 77°, \chi' = 20°$ (solid, blue line) and experimental (dashed, red line) OKE signals: (a) time traces, (b) spectral densities. Both traces exhibit strong modulation due to the homodyne-detected intensity with beating periods of 16.7 and 8.3 ps. The heterodyne part encodes the oscillation period of 94 fs as the superimposed small-amplitude modulation. The experimental trace was moved by −4.8 ps to compensate for the phase shift. The baseline of the time trace is shifted to zero by subtracting the local oscillator intensity C^2. Dephasing is set to $\gamma^{-1} = 45$ ps.

difference frequency corresponding to the 17-ps oscillation is resolved at 2 cm^{-1} in the inserted low-energy region of the spectrum. The signal intensity has a negligible contribution from the 8-ps (4 cm^{-1}) component due to the heavy weight on central $|M| = 2$ component.

Figure 7 shows how the state emergence has changed when inverted by the choice of $\chi' = 20°$ for the otherwise same parameters $\sigma = 130$ fs and $C = 0.003$. The idea is to suppress the $M = \pm 2$ state dominance seen in Fig. 6. The trace now displays more complicated structure. The homodyne-detected intensity shows oscillation periods at both 8.3 and 16.7 ps, since the relative $|M|$ distribution is counterbalanced. The shorter interval now follows from the increased significance of $\tau_{\rm osc} = 2\pi/(\omega_0 - \omega_1)$ contribution. With these angles $\theta' = 77°$ and $\chi' = 20°$, we also find a good agreement with an experimental trace chosen for illustrative comparison, shown in Fig. 7. The experimental trace was produced by $\sigma = 130$ fs probe pulse and recorded at 386 nm, i.e., anti-Stokes shifted from the probe center at 391 nm [29]. The experimental trace (a) and spectrum (b) are faithfully reproduced when $\gamma^{-1} = 45$ ps is used for the dephasing time in the simulation (halved from that in Fig. 6). The probe pulse length was set to 130 fs, which matches the one used in measurements [29], and $C = 0.003$ as before. We observe the fast oscillation of the heterodyne part with intensity modulated by the slow homodyne part showing the 8.3- and 16.7-ps intervals. The first recurrence in the experimental trace was shifted to $\tau = 0$ (by −4.8 ps) in order to maximally overlap with the theory. Although the agreement appears to be nice, the delayed first intensity maximum in the experiment indicates relative phase shifts between the M components that are different from what is obtained with the $\theta' = 77°, \chi' = 20°$ setting. At later times the experimental trace is shifting slightly out of phase as the oscillation periods increase in the homodyne part, which may be due to inaccurate delay-stage calibration. Correspondingly, the frequency differences are expected to decrease. The effect is reflected in the skewed line shapes of the transitions shown in Fig. 7(b), which also reveals a mismatch between the $M = 0$ spectral weights.

The spectrally dispersed version of the above calculated trace (see Fig. 7) is given in Fig. 8, where the signal emerges Stokes and anti-Stokes shifted from the 391-nm probe center as calculated by Eq. (49). The homodyne contribution

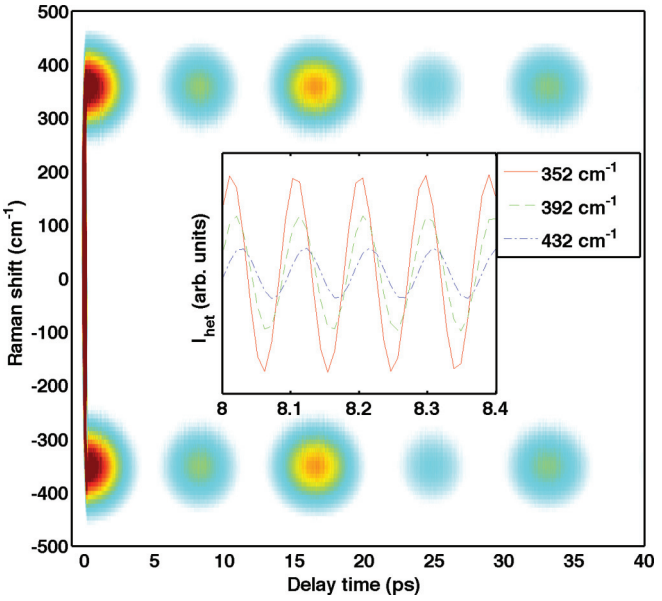

FIG. 8. (Color online) Two-dimensional pump-probe OKE signal for $\theta' = 77^\circ$ and $\chi' = 20^\circ$. Stokes and anti-Stokes radiations emerge at negative and positive wave numbers, respectively, relative to the probe center. The heterodyne-detected response is best observed as the fine structure at the slowly beating homodyne part. Inserted is a 400-fs time slice for three cuts within the anti-Stokes branch, showing the phase shift due to the negative chirp of the probe pulse.

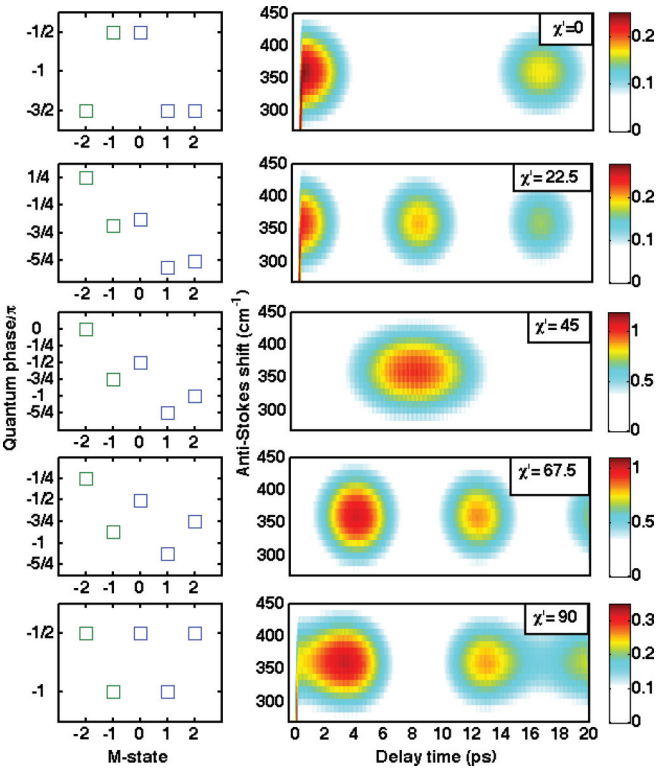

FIG. 9. (Color online) Impact of the quantum phase on 2D spectrograms. (Left panels) Phases of the $2M$ components after the 80-fs pump pulse with $\theta' = 77^\circ$. (Right panels) Anti-Stokes side of the pump-probe OKE signals.

dominates the appearance of the signal, which peaks at 396 nm (-355 cm^{-1}) and 386 nm ($+355$ cm^{-1}), respectively. The temporal signal oscillation patterns are identical in both branches. The heterodyne component is seen to texture the signal on top of the major pattern. The fast-modulation intensity stripes are slightly tilted by the value of $c' = -45$ ps^{-2} used for the chirp rate. The inset shows the effect of the probe chirp more closely. Only the heterodyne part is plotted here so the oscillation is around zero. It should be noted that the location of the heterodyne part intensity maximum results from the product of the local oscillator and the signal field: $E^*_{\rm lo}(\omega)E_s(\omega)$. Therefore, the modulation amplitude weakens as the difference from the probe center increases for the cuts shown at 352, 392, and 432 cm^{-1}. The probe chirp and broad-shaped bandwidth of the local oscillator [Eq. (50)] are necessary to have the heterodyne part overlapping with the homodyne part of the signal.

More detailed account for the effect of quantum phase factors between the components is given in Fig. 9. In the left column, we quantify the effect of angle $\chi' = 0^\circ$–90° on the phases φ_M in the roton packet. In the right column, the emergence of quantum beats in the homodyne part of the total signal field is demonstrated. We remind the reader that the wave-packet amplitudes in Fig. 4 are not affected by the variation of χ'; the $\theta' = 77^\circ$-set ratio of 0.69:1.44:1 for the $|M|$ values 1:2:0, respectively, remains through the Fig. 9 columns. We shortened the pump duration to 80 fs in order to avoid the resetting of phases at the Rabi period. The probe was negatively chirped as above. The top panel corresponds to the case shown in Fig. 6, where the intensity maximum was seen at $\tau = 0$. The situation is not markedly changed when going to $\chi' = 22.5^\circ$, near the condition of Figs. 7 and 8, except that the 8-ps period (ω_{01}) in addition to the 17-ps period (ω_{21},ω_{02}) becomes visible. In order to have a shifted first signal peak, higher angles are needed. For example, the $\chi' = 67.5^\circ$ panel appears to satisfactorily represent the chosen experimental trace, where the first peak was located at 4.8 ps.

V. DISCUSSION

Since hydrogen molecules are quite special among the literature on intense-field alignment [69], we decided to explicitly cover the case, although the alignment properties can be extracted from general, molecule-nonspecific formulations [2]. Instead of a broad wave packet like that in N_2, here the molecular parameters together with the low temperature render a very limited alignment effect and a trivial state space structure. It was anticipated that, due to the pulse duration of 140 fs, the rotational coherence was likely just at the limit of detection [27]. The field-free alignment is revisited by comparing gaseous p-H_2 with N_2 that essentially differ by the rotational constant, nuclear spin, and the anisotropy of polarizability. The key alignment parameters like the pulse duration per rotational time and the Rabi frequencies are, in p-H_2, orders of magnitude off from what have been seen with heavier molecules. Based on the numerical evaluations, the measurements should indeed be near the detection limit with the 140–160-fs-long pump pulses. Noting that the rotational period $(1/2B_0c)$ for p-H_2 is ca. 280 fs, the time scale approaches that of the static, adiabatic regime of intense-field

alignment. However, the successful detections [27,29] of the roton dynamics emphasize the high Raman gain effect in the solid that compensates for the signal weakness.

It is clear from the above considerations that the appearance of the signal in terms of the relative weights of the M states is coincidental in experiments. The χ' orientation is changing from sample to sample and from one laser focus spot or volume to another, rendering the state resolution in ambiguity. To unravel wave-packet compositions in experimentally observed time traces and their Raman spectral densities, we can search correspondences by varying the angular space. To illustrate the concept, we compared a simulated trace to an experimental signal which was a spectrally selected cut from a dispersed emission. To reproduce the experiment as a whole, the signal simulation must be switched to a time-integrated, frequency-resolved coherent Raman scattering type, where details of the probe and local oscillator fields have to be considered. For example, the wavelength dependence of the extinction coefficient introduces an intensity minimum for the local oscillator at the probe center. The Raman spectral density shows three frequencies in agreement with the theory of the solid p-H_2; i.e., the levels $|M| = 0,1,2$ are resolved. Another aspect is the ambiguity in the phases, manifest in time domain signals. We introduced a time shift to match with the picked experimental curve. The signal intensity exhibits peaks when the oscillators are rephased, and one might consider estimating the temporal shift in the experiment from the expression

$$I_{\mathrm{hom}}(\tau) \propto jk\cos(\omega_{21}\tau+\varphi_{21}) + kl\cos(\omega_{02}\tau+\varphi_{02}) + jl\cos(\omega_{01}\tau+\varphi_{01}), \quad (52)$$

where the coefficients j,k,l represent the roton amplitudes. For example, at $\tau = 4.74$ ps the signal I_{hom} shows a maximum as in the experiment if $\varphi_{21} = 10\pi/7$, $\varphi_{02} = -4\pi/7$, and $\varphi_{01} = 6\pi/7$. The emergence of M states in the Fourier transform of the signal is delicate with respect to changes of the crystal orientation, and it is a challenging task to seek a perfect match. We note that it is easier to reproduce the experimental trace by fitting a suitably parametrized set of cosine functions than by simulating. When the signal is analyzed with damping terms $\exp(-\gamma_{21}\tau)$, etc., augmented in Eq. (52), the experiment reveals $|M|$-specific dephasing times [30]: 132, 114, and 82 ps in order of increasing energy. The simulation and Eq. (28) indicate, however, that all five M components are needed instead of just the three $|M|$. The roton phase information in Fig. 9 cannot be directly used, since the signal acquires additional phase terms through the detection [see Eq. (46)], which is quite complicated to expand. However, the quantum phase and Fig. 9 give the first answer to the question of origin of temporal shifts of the first signal maxima observed in experiments [29,30].

As the outlook we note the importance in unraveling the details in dispersed detection of the birefringence signal from crystalline parahydrogen samples. The experiments resolve the OKE signal into Stokes and anti-Stokes shifted branches of radiation and produce 2D spectrograms. According to the third-order polarization mechanism, the two nonresonant, intramolecular pathways between ket and bra side excitations should show an in-phase response, as verified theoretically and experimentally for $CHCl_3$ [52,70]. The present evaluations faithfully reproduce the spectrogram images reported for p-H_2 [30]. Interestingly, in some samples there were differences between the branches [71], which calls for a revised theoretical description. With the present investigation we cannot rule out whether the detected differences between Stokes and anti-Stokes branches arise from the properties of the probe pulse or the parahydrogen crystal itself. We included both the chirp of the probe and the amplitude modulation of the local oscillator but did not observe significant phase, amplitude, or signal modulation asymmetry between the pathways. A more probable cause of the effect is that, despite the lower intensity, the Raman cross section is higher for the frequency-doubled probe than for the pump. Thus, the probe pulse might not have been just a nonintrusive spectator as it was considered in the simulations. The pump and probe pulse power dependencies and corresponding nonlinear effects are beyond the present analysis. So a challenge remains in explaining whether the Stokes and anti-Stokes shifted branches of the scattered probe can show different dynamics via higher order Raman transitions. Further studies on rotationally equivalent orthodeuterium could be helpful to rule out the solid-state origin of the effect.

VI. CONCLUSIONS

The paper shows how experimental femtosecond pump-probe OKE signals from solid p-H_2 can be computationally reproduced. We obtained a functional form of the molecular alignment degree, which reflects the induced birefringence and rotational dynamics. The rotational coherence shows up as the signal oscillation during the pump-probe time delay, and we report the geometrical dependencies affecting the outcome. The beating patterns in time-resolved traces are dictated by the relative orientation (θ', χ') of the laser beam and the orientation of the single crystallites. Control over the population of the states that constitute the roton wave packet can be obtained by focusing the pump laser beam on a specific spot on the surface plane of the solid parahydrogen crystal. The angle θ' is then approximately known and it dictates the M-state amplitudes. Further experiments should be systematically conducted to verify the present predictions on angle dependence. The focusing does not offer a control over the single crystallites that are oriented randomly along the beam path in the cylindrical chamber that hosts the solid sample. However, the value of χ' can be deduced from the signal trace with the help of the presented theory. Although the experiments manifest the large Raman gain for solid p-H_2, we predict that shortening the pump-pulse duration into nonadiabatic regime would significantly enhance the signal intensity and emergence of roton dynamics. The derived theory and presented analysis exemplify the geometrical manipulation of rotational Raman spectral densities as detected by the nonlinear pump-probe spectroscopy, and the results can be used in assignments of corresponding 2D spectrograms.

ACKNOWLEDGMENTS

The authors would like to thank Professor N. Schwentner and Professor D. Anderson for carefully reading the present

manuscript and for sending the experimental paper prior to publication. F. Königsmann is acknowledged for sending the experimental data and T. Järvinen is thanked for the help with density matrix propagation codes. Support from the Academy of Finland through Decision No. 124974 is gratefully acknowledged.

[1] H. Stapelfeldt and T. Seideman, Rev. Mod. Phys. **75**, 543 (2003).
[2] T. Seideman and E. Hamilton, Adv. At. Mol. Opt. Phys. **52**, 289 (2005).
[3] D. Daems, S. Guérin, E. Hertz, H. R. Jauslin, B. Lavorel, and O. Faucher, Phys. Rev. Lett. **95**, 063005 (2005).
[4] M. Artamonov and T. Seideman, J. Chem. Phys. **128**, 154313 (2008).
[5] M. Lapert, E. Hertz, S. Guérin, and D. Sugny, Phys. Rev. A **80**, 051403(R) (2009).
[6] M. Z. Hoque, M. Lapert, E. Hertz, F. Billard, D. Sugny, B. Lavorel, and O. Faucher, Phys. Rev. A **84**, 013409 (2011).
[7] S. Zhdanovich, A. A. Milner, C. Bloomquist, J. Floß, I. S. Averbukh, J. W. Hepburn, and V. Milner, Phys. Rev. Lett. **107**, 243004 (2011).
[8] M. Lapert, R. Tehini, G. Turinici, and D. Sugny, Phys. Rev. A **78**, 023408 (2008).
[9] K. Nakajima, H. Abe, and Y. Ohtsuki, J. Phys. Chem. A **116**, 11219 (2012).
[10] M. Lapert, S. Guérin, and D. Sugny, Phys. Rev. A **83**, 013403 (2011).
[11] J. P. Cryan, J. M. Glownia, D. W. Broege, Y. Ma, and P. H. Bucksbaum, Phys. Rev. X **1**, 011002 (2011).
[12] J. Itatani, J. Levesque, D. Zeidler, H. Niikura, H. Pépin, J. C. Kieffer, P. B. Corkum, and D. M. Villeneuve, Nature (London) **432**, 867 (2004).
[13] T. Kanai, S. Minemoto, and H. Sakai, Nature (London) **435**, 470 (2005).
[14] F. Filsinger, G. Meijer, H. Stapelfeldt, H. N. Chapman, and J. Küpper, Phys. Chem. Chem. Phys. **13**, 2076 (2011).
[15] T. Brixner and G. Gerber, ChemPhysChem. **4**, 418 (2003).
[16] P. Nuernberger, G. Vogt, T. Brixner, and G. Gerber, Phys. Chem. Chem. Phys. **9**, 2470 (2007).
[17] S. Ramakrishna and T. Seideman, Phys. Rev. Lett. **95**, 113001 (2005).
[18] S. Ramakrishna and T. Seideman, J. Chem. Phys. **124**, 034101 (2006).
[19] T. Kiljunen, B. Schmidt, and N. Schwentner, J. Chem. Phys. **124**, 164502 (2006).
[20] J. Peng, T. C. Castonguay, D. F. Coker, and L. D. Ziegler, J. Chem. Phys. **131**, 054501 (2009).
[21] J. Lindgren, A. Olbert-Majkut, M. Pettersson, and T. Kiljunen, J. Chem. Phys. **137**, 164310 (2012).
[22] T. Kiljunen, M. Bargheer, M. Gühr, and N. Schwentner, Phys. Chem. Chem. Phys. **6**, 2185 (2004).
[23] T. Kiljunen, B. Schmidt, and N. Schwentner, Phys. Rev. Lett. **94**, 123003 (2005).
[24] T. Kiljunen, B. Schmidt, and N. Schwentner, Phys. Rev. A **72**, 053415 (2005).
[25] D. Pentlehner, J. H. Nielsen, A. Slenczka, K. Mølmer, and H. Stapelfeldt, Phys. Rev. Lett. **110**, 093002 (2013).
[26] C. Sierens, A. Bouwen, E. Goovaerts, M. DeMazière, and D. Schoemaker, Phys. Rev. A **37**, 4769 (1988).
[27] F. Königsmann, M. Fushitani, N. Owschimikow, D. T. Anderson, and N. Schwentner, Chem. Phys. Lett. **458**, 303 (2008).
[28] J. van Kranendonk and G. Karl, Rev. Mod. Phys. **40**, 531 (1968).
[29] F. Königsmann, Ph.D. thesis, Freie Universität Berlin, Germany, 2012.
[30] F. Königsmann, N. Schwentner, and D. T. Anderson, Phys. Chem. Chem. Phys. **15**, 17435 (2013).
[31] M. Leblans, A. Bouwen, C. Sierens, W. Joosen, E. Goovaerts, and D. Schoemaker, Phys. Rev. B **40**, 6674 (1989).
[32] E. Goovaerts, X. Y. Chen, A. Bouwen, and D. Schoemaker, Phys. Rev. Lett. **57**, 479 (1986).
[33] M. Vanhimbeeck, H. DeRaedt, A. Lagendijk, and D. Schoemaker, Phys. Rev. B **33**, 4264 (1986).
[34] R. Sliter and A. F. Vilesov, J. Chem. Phys. **131**, 074502 (2009).
[35] I. F. Silvera, Rev. Mod. Phys. **52**, 393 (1980).
[36] B. Lavorel, O. Faucher, M. Morgen, and R. Chaux, J. Raman Spectrosc. **31**, 77 (2000).
[37] P. W. Dooley, I. V. Litvinyuk, K. F. Lee, D. M. Rayner, M. Spanner, D. M. Villeneuve, and P. B. Corkum, Phys. Rev. A **68**, 023406 (2003).
[38] K. F. Lee, D. M. Villeneuve, P. B. Corkum, and E. A. Shapiro, Phys. Rev. Lett. **93**, 233601 (2004).
[39] M. Renard, E. Hertz, B. Lavorel, and O. Faucher, Phys. Rev. A **69**, 043401 (2004).
[40] S. Fleischer, I. S. Averbukh, and Y. Prior, Phys. Rev. Lett. **99**, 093002 (2007).
[41] Y.-H. Chen, S. Varma, A. York, and H. M. Milchberg, Opt. Express **15**, 11341 (2007).
[42] R. de Nalda, C. Horn, M. Wollenhaupt, M. Krug, L. Bañares, and T. Baumert, J. Raman Spectrosc. **38**, 543 (2007).
[43] T. Suzuki, Y. Sugawara, S. Minemoto, and H. Sakai, Phys. Rev. Lett. **100**, 033603 (2008).
[44] B. K. McFarland, J. P. Farrell, P. H. Bucksbaum, and M. Gühr, Science **322**, 1232 (2008).
[45] J. P. Cryan, P. H. Bucksbaum, and R. N. Coffee, Phys. Rev. A **80**, 063412 (2009).
[46] S. Fleischer, Y. Khodorkovsky, Y. Prior, and I. S. Averbukh, New J. Phys. **11**, 105039 (2009).
[47] N. Owschimikow, F. Königsmann, J. Maurer, P. Giese, A. Ott, B. Schmidt, and N. Schwentner, J. Chem. Phys. **133**, 044311 (2010).
[48] N. K. Owschimikow, Ph.D. thesis, Freie Universität Berlin, Germany, 2011.
[49] C. W. Freudiger, M. B. J. Roeffaers, X. Zhang, B. G. Saar, W. Min, and X. S. Xie, J. Phys. Chem. B **115**, 5574 (2011).
[50] M. Morgen, W. Price, L. Hunziker, P. Ludowise, M. Blackwell, and Y. Chen, Chem. Phys. Lett. **209**, 1 (1993).
[51] M. Morgen, W. Price, P. Ludowise, and Y. Chen, J. Chem. Phys. **102**, 8780 (1995).
[52] S. Constantine, Y. Zhou, J. Morais, and L. D. Ziegler, J. Phys. Chem. A **101**, 5456 (1997).

[53] K. P. Huber and G. Herzberg, *Molecular Spectra and Molecular Structure. IV. Constants of Diatomic Molecules* (Van Nostrand Reinhold, New York, 1979).
[54] J. van Kranendonk, Physica **25**, 1080 (1959).
[55] M. Okumura, M.-C. Chan, and T. Oka, Phys. Rev. Lett. **62**, 32 (1989).
[56] N. Owschimikow, B. Schmidt, and N. Schwentner, Phys. Rev. A **80**, 053409 (2009).
[57] R. N. Zare, *Angular Momentum* (Wiley, New York, 1988).
[58] A. J. Stone, *The Theory of Intermolecular Forces* (Oxford University Press, Oxford, 1997).
[59] V. G. Manzhelii and M. A. Strzhemechny, in *Physics of Cryocrystals*, edited by V. G. Manzhelii and Y. A. Freiman (AIP, Woodbury, NY, 1997).
[60] F. Baas and K. D. van den Hout, Physica A **95**, 579 (1979).
[61] J. O. Hirschfelder, C. F. Curtiss, and R. B. Bird, *Molecular Theory of Gases and Liquids* (Wiley, New York, 1954).
[62] S. Mukamel, *Principles of Nonlinear Optical Spectroscopy* (Oxford University Press, New York, 1995).
[63] Y. J. Yan and S. Mukamel, J. Chem. Phys. **94**, 997 (1991).
[64] M. Cho, M. Du, N. F. Scherer, G. R. Fleming, and S. Mukamel, J. Chem. Phys. **99**, 2410 (1993).
[65] V. Renard, M. Renard, S. Guérin, Y. T. Pashayan, B. Lavorel, O. Faucher, and H. R. Jauslin, Phys. Rev. Lett. **90**, 153601 (2003).
[66] R. H. Stolen and C. Lin, Phys. Rev. A **17**, 1448 (1978).
[67] T. Seideman, J. Chem. Phys. **115**, 5965 (2001).
[68] S. J. Yun, C. M. Kim, J. Lee, and C. H. Nam, Phys. Rev. A **86**, 051401 (2012).
[69] M. N. Slipchenko, B. D. Prince, S. D. Ducatman, and H. U. Stauffer, J. Phys. Chem. A **113**, 135 (2009).
[70] L. D. Ziegler, R. Fan, A. E. Desrosiers, and N. F. Scherer, J. Chem. Phys. **100**, 1823 (1994).
[71] N. Schwentner (private communication).